12-2020

Effects of Ca Doping on Structural and Optical Properties of PZT Nanopowders

K. H. Omran
South Valley University

M. Mostafa
South Valley University

M. S. Abd El-sadek
South Valley University

O. M. Hemeda
Tanta University

R. Ubic
Boise State University

Publication Information

Omran, K. H.; Mostafa, M.; Abd El-sadek, M. S.; Hameda, O. M.; and Ubic, R. (2020). "Effects of Ca Doping on Structural and Optical Properties of PZT Nanopowders". *Results in Physics, 19*, 103580-1 - 103580-11.
https://doi.org/10.1016/j.rinp.2020.103580

Results in Physics 19 (2020) 103580

Contents lists available at ScienceDirect

Results in Physics

journal homepage: www.elsevier.com/locate/rinp

Effects of Ca doping on structural and optical properties of PZT nanopowders

K.H. Omran [a,b,*], M. Mostafa [b,c], M.S. Abd El-sadek [a], O.M. Hemeda [d], R. Ubic [e]

[a] Nanomaterials Lab., Physics Department, Faculty of Science, South Valley University, Qena 83523, Egypt
[b] Laser Tech. & Environment Lab., Physics Department, Faculty of Science, South Valley University, Qena 83523, Egypt
[c] Physics Department, College of Science, Jouf University, Sakaka, Saudi Arabia
[d] Physics Department, Faculty of Science, Tanta University, Egypt
[e] Micron School of Materials Science & Engineering, Boise State University, Boise, USA

ARTICLE INFO

Keywords:
Pechini method
nano $PbCaZrTiO_3$
Band gap
Rietveld method
Modified tolerance factor
PZT

ABSTRACT

The influence of the addition of calcium ions (Ca^{2+}) in the $Pb_{(1-x)}Ca_xZr_{0.52}Ti_{0.48}O_3$ system (PCZT) for x = 0.05, 0.10, 0.15, 0.20, and 0.25 on the structural and optical properties was systematically studied. The compositions were synthesized through a polymerized-complex approach based on the Pechini polymeric precursor route. The solubility limit of calcium ions within the PCZT lattice is in between x = 0.10 and x = 0.15, at which a $CaTiO_3$ secondary phase is detected. The Goldschmidt tolerance factors, modified tolerance factors, and the effective vacancy sizes were all estimated for the synthesized nanopowders. While the Goldschmidt tolerance factors suggest the formation of a distorted perovskite structure, the values of the modified tolerance factor were extremely close to unity, indicating a strong stable ferroelectric perovskite structure. The optical band gap was found to decrease with calcium concentration to a minimum at x = 0.20 and then slightly increase at x = 0.25.

Introduction

Lead zirconate titanate (PZT) remains the most important commercial piezoelectric perovskite ceramic material [1,2]. It is characterized by a large range of properties and hence is used in a variety of commercial applications including hydroacoustic devices, microphones, nonvolatile memories, force sensors, infrared sensors, ultra-large-scale-integration (ULSI), and acceleration transducers [3–6]. Although the scientific community has been searching for innovative Pb-free piezoelectric materials with characteristics comparable to PZT for health and environmental reasons [7–9], recent comparative environmental impact studies carried out by Ibn-Mohammed et al. [7–9] showed that PZT could actually be more environmentally benign than a number of the current Pb-free alternatives such as potassium sodium niobate (KNN) and bismuth sodium titanate (BNT).

PZT can be made in various crystallographic forms, depending on composition, and these forms control the consequent electrical and physical properties. In general, it adopts a variation of the well-established perovskite structure with the basic stoichiometry ABO_3, where the Pb^{2+} ion occupies the A site and both the Zr^{4+} and Ti^{4+} ions share the B site [1]. It is frequently prepared via a conventional solid-state synthesis method by combining antiferroelectric lead zirconate ($PbZrO_3$) with ferroelectric lead titanate ($PbTiO_3$) [10]. The most important PZT-type compositions are those near the morphotropic phase boundary (MPB), around $PbZr_{0.52}Ti_{0.48}O_3$, where both rhombohedral (Zr-rich) and tetragonal (Ti-rich) phases coexist [11,12]. Other recent studies [12–14] reported the coexistence of tetragonal, rhombohedral, and monoclinic room-temperature phases at the MPB.

Lead-based piezoelectric materials mostly contain >60 wt% lead, which might be released to the environment in particular via the volatilization of lead oxide during the calcination and sintering stages of the production process [7,9]. The resulting lead and oxygen vacancies make it difficult to precisely control the final stoichiometry [15] and influence the piezoelectric properties [10,15–18]. These phenomena, as well as the environmental consequences of PbO volatilization, are commonly associated with PZT materials. Coupled with the growing need for nanoscale ferroelectric capacitors for ULSI memories [5], these issues have pushed researchers to explore alternative methodologies to synthesize ceramic substances with uniform homogeneity and nano particles at fairly low calcination temperatures [19,20]. For instance, the polymeric precursor route, known as the Pechini method [21], has been extensively utilized to synthesize ferroelectric materials [22–24] as it

* Corresponding author.
E-mail address: khaled.omran@svu.edu.eg (K.H. Omran).

https://doi.org/10.1016/j.rinp.2020.103580
Received 8 September 2020; Received in revised form 27 October 2020; Accepted 1 November 2020
Available online 5 November 2020

enables the production of nano particles with exceptionally uniform size distributions [22,25] and good chemical homogeneity. It also gives the ability to control the stoichiometry through simple procedures and relatively low-cost precursors.

Indeed, the commercial applications of ceramics depend significantly on their characteristics, including crystal structure, homogeneity, stoichiometry, grain size, and grain size distribution [26,27]. The crystal structure of perovskite materials can be changed considerably by doping on A and/or B sites, thus tuning the electrical and physical properties [28,29]. Similarly, PZT material could be modified by doping with either isovalent or heterovalent ions on either Pb and/or Zr/Ti sites, resulting in tailored properties required for specific applications [30,31].

In earlier studies, PZT materials have been prepared with various dopants such as La^{3+}, Bi^{3+}, Nd^{3+}, etc. as donor dopants on the A site, substituting for Pb^{2+} [1,32], and Nb^{5+}, W^{6+}, V^{5+}, etc. substituting for Ti^{4+}/Zr^{4+} on the B site [33,34]. For instance, improved dielectric and piezoelectric properties were achieved in ceria-doped (A site) PZT and niobium-doped (B site) PZT materials [31,35]. Similarly, A-site doping with Ba^{2+}, Cd^{2+} and Sr^{2+} showed enhanced ferroelectric and piezoelectric behaviour [36,37]. In addition, Kulcsar [38], Cerqueira et al. [39], Tawfik et al. [40], Sachdeva et al. [41], and Kour et al. [42,43] have studied the doping process of Ca^{2+} in $Pb_{1-x}Ca_x(Zr_yTi_{1-y})O_3$ for $x \leq 0.10$ and found that the dielectric and the piezoelectric properties improved with the addition of Ca^{2+}. Nasar et al. [44] reported a strong agglomeration tendency with an increase in porosity and particle size at $x = 0.05$.

Despite the extensive work on PZT material, relatively few attempts have been reported to reduce its lead content and hence minimize the health and environmental concerns. For this reason, a systematic report on the effect of partially substituting Pb^{2+} with Ca^{2+} is reported here, including consequent effects on the microstructural and optical features of PCZT nanopowders.

Experimental

Nanopowders of $Pb_{(1-x)}Ca_xZr_{0.52}Ti_{0.48}O_3$ (PCZT), where $x = 0.05$, 0.10, 0.15, 0.20 and 0.25, were synthesized by simple procedures based on the Pechini method. Analytical grade lead (ll) nitrate, zirconium oxynitrate, calcium acetate, titanium butoxide, ammonia, and citric acid were utilized as raw materials. To begin a solution of 40 wt% of citric acid was prepared. Afterwards, the stoichiometric weight of lead, calcium, and zirconium precursors was dissolved in distilled water to form a clear solution. Next, the appropriate quantity of titanium butoxide was dissolved in 30 ml of 40 wt% citric acid at 50 °C. Once a clear solution of titanium precursor was obtained, the prepared precursor solutions (lead, calcium, and zirconium precursors) were modified using a few droplets of a 40 wt% citric acid then added to the titanium precursor solution and mixed together. After a transparent solution was formed, the pH was raised to 4, where the solution lifts under continuous stirring in a covered vial for 2 h. Later, the solution was lifted to evaporate at a temperature of 80 °C to form the gel, which was then further lifted to dry at 180 °C to obtain the dried black powder. Lastly, the formed dried gel was calcined at 750 °C, as recommended [44–46], to enhance the crystallization and to form the desired nanomaterial. The details of the preparation process are shown schematically in Fig. 1 and can be found in previous published work [24].

Thermogravimetric analysis and differential scanning calorimetry (Linseis, STA PT-1000) were employed to examine the thermal behaviour of the dried gel using a heating rate of 10 °C/min. The phase identification of the prepared specimens was performed using X-ray powder diffraction (Philips, PW 1710) using Cu Kα (λ = 1.5406 Å) radiation. The XRD data were recorded over the angular range of 20–90° 2theta with step size and a scan speed of 0.02° and 0.05° min^{-1}, respectively. Full-profile fit (LeBail methodology) for the XRD data was undertaken using FullProf program to accurately assess the full width at half maximum of the peaks to be used in the calculation of crystallite size and lattice strain via the Williamson-Hall method. Crystallographic details involving phase fraction, crystal structure, and lattice parameters were acquired utilizing Rietveld structure refinement of the X-ray diffraction data using the FullProf software package. The Fourier transmission infrared (FT-IR) spectrum of the synthesized nanopowder was recorded over the wavenumber range 400–4000 cm^{-1} (JASCO, FT-IR 4100). Diffuse reflectance measurements were obtained with a spectrophotometer (JASCO, V-670) in the wavelength range 200–900 nm to determine the optical band gap of the prepared nanopowders via

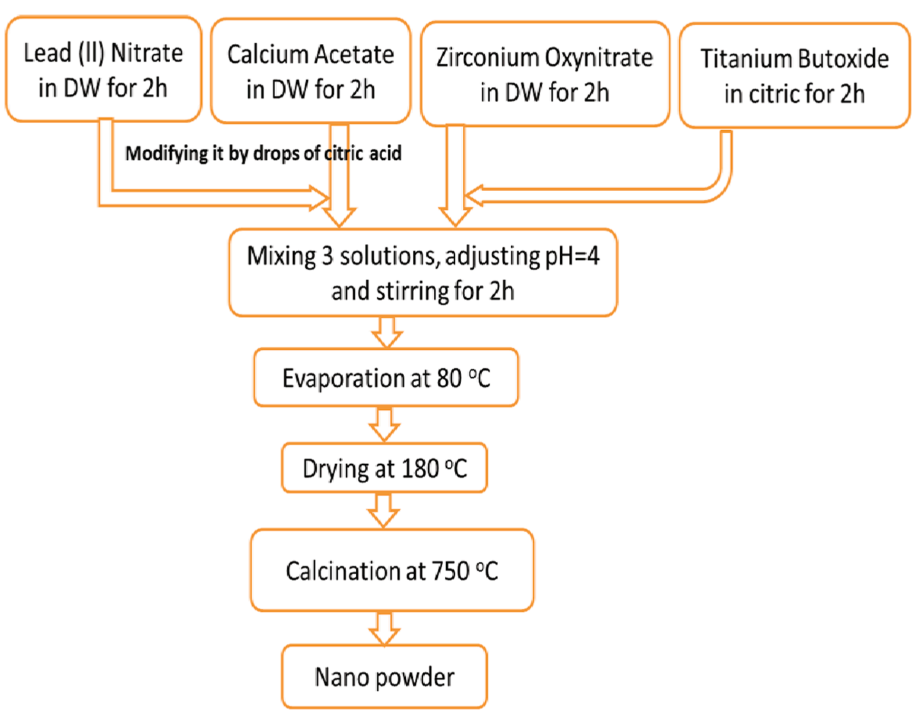

Fig. 1. Schematic representation of the preparation procedures of PCZT nanopowders.

the Kubelka-Munk formalism. Scanning electron microscopy (JEOL, JSM 5500LV) and transmission electron microscopy (JEOL, JEM 1010) were employed to reveal the microstructure of the synthesized nanopowders whereas the elemental analysis was studied using energy dispersive spectroscopy (Oxford Instruments, ISIS Link).

Results and discussion

TGA and DSC analysis

Thermogravimetric analysis (TGA) and differential scanning calorimetry (DSC) were utilized for investigating the physical features of the black dried gel as a function of the temperature, and the results are presented in Fig. 2. About 20 mg of the dried powder was heated in alumina pans from room temperature to 700 °C with a heating rate of 10 °C/min. Three main regimes of weight loss are evident in the TGA curve. Initially, the weight loss slightly reduced with temperature up to 225 °C, with about 5% mass loss. This initial stage may be attributed to the release of the adsorbed water [47,48]. The next mass loss occurred in a temperature ranging between 225 °C and 480 °C, wherein a weight loss of about 25% occurred. This major mass loss might be attributed to the combustion of the organic groups components [49,50]. The last regime, during which about 15% of the weight was lost, occurred in a temperature ranging between 480 °C and 550 °C, indicating the decomposition process which leads to the PCZT formation [51,52]. These stages of weight loss were reflected in the DSC trace as exothermic peaks. Three exothermic peaks are visible at 150 °C, 270 °C, and 520 °C. The TGA/DSC results clearly demonstrate that the mass loss remains nearly steady above 600 °C, implying that the calcination temperature must be higher than 600 °C in order to form the desired phase structure.

Structure studies

X-ray diffraction analysis

Fig. 3 presents the XRD patterns of $Pb_{(1-x)}Ca_xZr_{0.52}Ti_{0.48}O3$ (PCZT) nanopowders calcined at 750 °C with x = 0.05, 0.10, 0.15, 0.20, and 0.25. It is obvious from the XRD patterns that all of the powder samples exhibit the characteristic peaks of tetragonal PZT with some PbO secondary phase, which is consistent with the previously established observations for PZT nanopowders [24,51,53–56]. It is noteworthy that the XRD patterns of the nanopowder samples with x = 0.15, 0.20, and 0.25 indicate the evolution of an orthorhombic $CaTiO_3$ phase, which gets more evident and its orientation peaks grow in intensity with rising

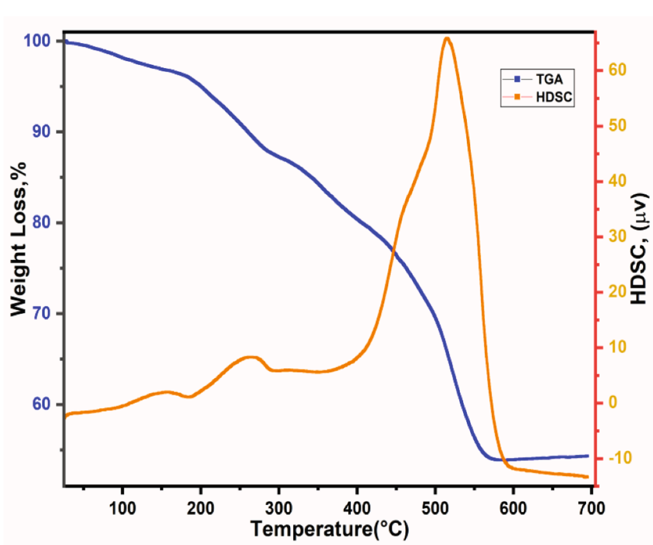

Fig. 2. TGA/DSC curves of PCZT dried gel for x = 0.05.

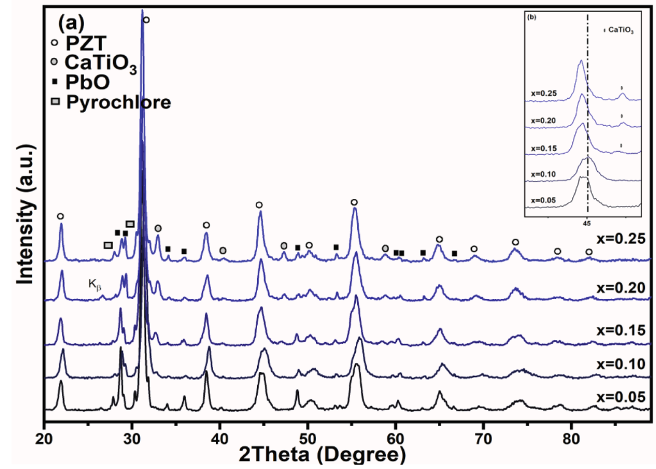

Fig. 3. (a) Typical x-ray diffractograms of $Pb_{(1-x)}Ca_xZr_{0.52}Ti_{0.48}O_3$ nanopowders for x = 0.05, 0.10, 0.15, 0.20, and 0.25. Enlarged (b) presents the evolution of $CaTiO_3$ (220) peak and the shifting of (200) peak.

calcium amount. Moreover, the magnified XRD patterns, in Fig. 3 (b), obviously indicate the overlapping of the (002) and (200) reflections that are commonly utilized for distinguishing the tetragonal phase from rhombohedral and monoclinic phases [12,14]. It is also evidently demonstrate the development of the orthorhombic $CaTiO_3$ phase with the increase of Ca^{2+} concentration. The presence of a tiny amount of pyrochlore phase and orthorhombic PbO phase is revealed by the XRD analysis, which are observed in several previously published studies [56–58]. The observed small traces of PbO can be decomposed and can disappear through the increase in the calcination temperature and time [24,56], while the accompanied pyrochlore phase is usually formed as an intermediate phase during the evolution of PZT material and can be decomposed at higher temperatures [57–59].

It is important to demonstrate that the disappearance of Ca-related secondary phases in samples with x = 0.05 and 0.10 indicates that the calcium is completely diffused into the cell lattice of PZT to form a solid solution of PCZT, while the clear observation of the orthorhombic $CaTiO_3$ phase above x = 0.10 indicates that the Ca^{+2} is not thoroughly dissolved in the host throughout the calcination process [60,61]. It is also noteworthy that the samples with x = 0.05 and 0.10 clearly show shifts on the XRD peaks towards the higher 2theta values, which corresponds to lower cell constants and cell volume, whereas the samples with x > 0.10 show the most intensive peaks shift towards the lower 2θ value, which corresponds to larger lattice parameter and lattice volume. These results agree with the earlier reported observations [42,60]. Furthermore, the notable broadening of reflection peaks reflects the nanocrystalline features of the prepared powders and possible presence of microstrain [62].

The LeBail profile fitting approach was applied to the detected XRD data in order to accurately evaluate the broadening of peaks through isolating the overlapped peaks so that further precise calculations of the lattice size and the microstrain could be obtained. Additionally, the Rietveld structure refinement methodology was also applied to the XRD patterns in order to investigate the microstructure changes and to quantitatively evaluate the fraction percent of each existing phase with the variation of the Ca concentration.

Rietveld refinement. Rietveld structure refinements for the synthesized nanopowders were fulfilled through the use of FullProf software packages and high-quality collected XRD data in order to determine the fractional phase components percent as well as the various crystallographic properties. Fig. 4 presents the refinement pattarns of the synthesized PCZT nanopowders. Initially, the refinement procedures were carried out following the adoption of various needed information,

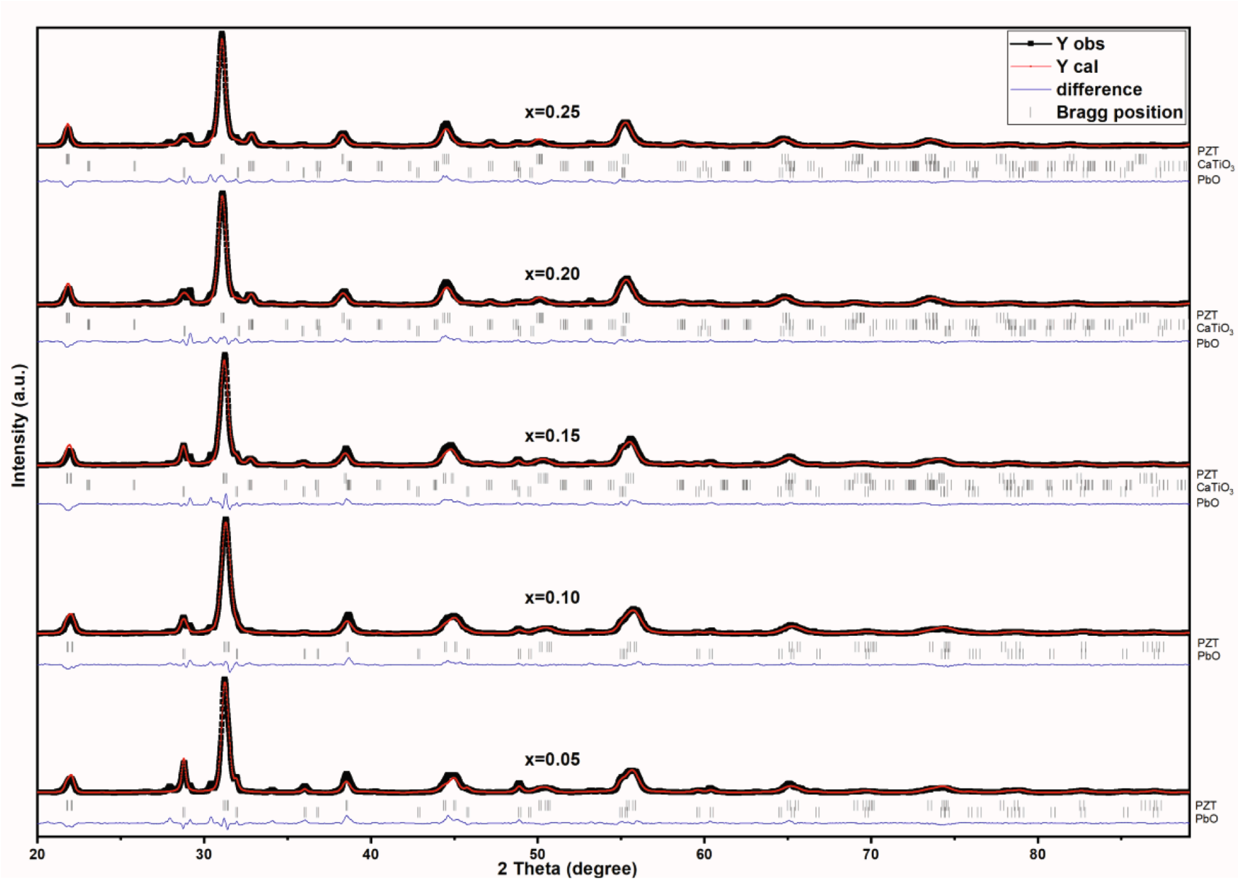

Fig. 4. Rietveld refined XRD patterns of the synthesized PCZT nanopowders.

including the structure information of the identified phases which are obtained from the cif files, the background that is identified as a linear interpolation of adjusted selected points, the peak profile function which is defined as Thompson-Cox-Hastings pseudo-Voigt (pV-TCH), and the determined instrumental resolution function (IRF). The IRF details were returned through employing the WinPlotr program using a detected XRD pattern from a reference specimen (Si) with the same identified measurement conditions.

The starting structure information of the tetragonal PZT, the tetragonal PbO, and the orthorhombic $CaTiO_3$ phases was obtained from COD ID #1526147, COD ID #9012698, and COD ID #2100812 files, respectively. At the beginning of the refinement, the zero shift, the scale factor, and the lattice parameters were sequentially refined, whereby a justifiable pattern was achieved. Afterwards, the refinement was proceeded with the instrumental parameters, the profile parameters, the background points, and the atomic coordinates for further improvement of the matching between the calculated and detected values. The refinement continued for all the parameters simultaneously till the best convergence was achieved, with no further improvements of the patterns or the conventional R factors. The quality of the refinement process was associated with the good agreement between the calculated and detected patterns in addition to the various mathematical factors, including the reliability (R) factors (profile R_p, weighted profile R_{wp}, and statistically expected R_{exp}), the goodness of fit (GOF), and the reduced chi2 (χ^2).

It is essential to point out that several aspects were taken into account while performing the refinement. Firstly, each refinement was initially performed several times with different identified phases. Secondly, the phases with a very small fractional amount (<2%) were not considered further in the refinement process. Thirdly, the calcium atom was assumed to occupy the lead (Pb) atomic position since the value of the ionic radius of rCa^{2+}=1.34 Å is close to that of rPb^{2+}=1.49 Å [1,42]. Furthermore, the sum of the occupancy of Pb and Ca atoms was constrained to 1 during the refinement process, which were later refined at the final stages. The several reliability (R) factors obtained (R_p, R_{wp}, and R_{exp}), χ^2, and the GOF of the refined samples are enlisted in supplementary **Table I**, whereas the obtained PZT unit cell parameters, c/a ratio, and the cell volume are gathered and included in Table 1. The obtained lattice constants values were found to be comparable with those established in previous studies [42,51,55,63].

Table 1 indicates that changes in the lattice parameters, cell volumes, and c/a ratio occurred in respect of the Ca concentration. The results demonstrate that the unit cell parameters and volume slightly lowered with the increase of the Ca concentration up to x = 0.10 and then dramatically increased with the increase of the Ca concentration. The reduction in the volume of the unit cell could happen as a result of the partial substitution of the smaller Ca^{2+} for the bigger Pb^{2+} cation species (rPb^{2+}=1.49 Å, rCa^{2+}=1.34 Å as per Shannon [64]) in the synthesized

Table 1
Unit cell constants, c/a ratio and volume of the PZT unit-cell.

x (Mole Fraction)	a (Å)	b (Å)	c (Å)	c/a	Vol (Å^3)
0.05	4.02915 (21)	4.02915 (21)	4.08041 (30)	1.0127	66.24
0.10	4.02358 (22)	4.02358 (22)	4.07631 (33)	1.0131	65.99
0.15	4.04001 (21)	4.04001 (21)	4.07959 (34)	1.0098	66.58
0.20	4.05904 (27)	4.05904 (27)	4.08383 (48)	1.0061	67.28
0.25	4.06370 (27)	4.06370 (27)	4.08356 (50)	1.0049	67.43

nanopowders, showing good agreement with previously published results [42,65], whereas the subsequent increase of the lattice volume with the further increase of Ca^{2+} concentrations could be attributed to the high distortion caused by the Pb^{2+} substitution and the evolution of the foreign $CaTiO_3$ phase along with the growth of various particle shapes and sizes [61,66]. Similar observations were reported elsewhere [67,68]. Moreover, it is believed that the formation of oxygen vacancies might also cause lattice expansion as observed in various compounds [65,69]. The microstructure studies (SEM and TEM images) support the assumption that the particle shapes and sizes are responsible for the observed lattice expansion. It is also noteworthy that the lowest R factors were observed for the sample with x = 0.10, where the greatest fractional percent of PZT was observed along with the highest observed diffused calcium inside the lattice.

The obtained fractional content of the individual phases is presented in Table 2. The results demonstrate that the fractional phase content of the tetragonal PZT significantly increased as x increased from x = 0.05 to x = 0.10, and then, it dramatically decreased as x increased, while the phase percent of the tetragonal PbO appeared with the maximum observed content at x = 0.05 and significantly decreased afterwards at x = 0.10; then, it slowly changed as x increased. On the other hand, the evolution of orthorhombic $CaTiO_3$ was recorded at x = 0.15 and dramatically increased afterwards as the Ca concentration increased. These results reveal that the calcium was completely diffused into the PZT lattice for samples with x = 0.05 and 0.10, whereas the other samples provided that the calcium ions tend to form the orthorhombic $CaTiO_3$ phase as a result of the limited solubility of Ca^{2+} in the solid crystal structure [60,61].

Particle size and strain analysis. The crystallite sizes and lattice microstrain of the synthesized nanopowders were estimated through the use of Williamson–Hall (WH) and Rietveld methods. It is known that the peak broadening of the XRD pattern might emerge due to several factors, including the small sizes of the investigated powder, the presence of lattice microstrain, and the instrumental contribution [62,70]. The size and strain evaluations using the isotropic strain methodology of the WH method were carried out following the instructions and equations previously reported [62,71]. For estimating the peak width correctly and for separating the overlapped diffraction peaks of the multiphase patterns, LeBail profile fitting was performed for all the investigated XRD patterns through the use of FullProf software package along with the matched cif files of the existing phases, which are identified by QualX software and acquired from the crystallographic open database (COD) for further adaptation as initial parameters in the fitting process. The full-widths at half-maximum (FWHM) implemented in the computation of crystallite size and lattice microstrain was corrected through the elimination of the instrumental broadening using the following equation [62]:

$$\beta_{hkl} = (\beta_{exp}^2 - \beta_{inst}^2)^{½} \tag{1}$$

where β_{exp} and β_{inst} are the experimental FWHM and the FWHM of well-crystallized reference material (here it is a silicon standard material), respectively. The Williamson-Hall (WH) plots for the studied samples of PCZT are shown in Fig. 5, while the results of the crystallite sizes and the

Table 2
Phase fraction percentage of each identified phase as obtained from Rietveld's powder structure refinement.

x (Mole Fraction)	PZT Fract. (%)	$CaTiO_3$ Fract. (%)	PbO-Tet. Fract. (%)
0.05	84.85 (0.50)	0	15.15 (0.17)
0.10	93.41 (0.47)	0	6.59 (0.10)
0.15	80.16 (0.51)	11.06 (0.40)	8.79 (0.12)
0.20	74.13 (0.49)	18.36 (0.46)	7.51 (0.12)
0.25	72.75 (0.47)	21.56 (0.45)	5.69 (0.10)

microstrains are summarized and presented in Table 3. It is notable that the evaluated values of the crystallite size and the microstrain obtained by the WH methodology first increased with the increase of x and decreased afterwards at x = 0.15, then significantly increased at x = 0.20, and slightly decreased at x = 0.25. Inversely, the crystallite size of the Rietveld method slightly decreased when x changed from x = 0.05 to x = 0.10 and increased afterwards at x = 0.15, then decreased at x = 0.20, and later slightly increased at x = 0.25, showing an opposite trend to the other utilized line profile methods. Moreover, the established WH size values were somewhat higher than the values of the Rietveld method. Furthermore, the lattice microstrain values of the Rietveld method increased initially and then decreased at x = 0.15 and gradually increased afterwards as x increased. It is important to highlight that the current observations imply that the crystallite size is not related to the Ca concentration which is contrasted with the observations of Sachdeva et al. and Kour et al., where the crystallite size decreased as the Ca concentration increased [41,42].

It is essential to point out that the calculated high strain values of the synthesized PCZT nanopowders compared to those of PZT nanopowders reported earlier [24] could be attributed to the presence of multiple phases in addition to the differences of the ionic radius of the foreign and substituted atoms which might enhance the distortion inside the lattice cell and hence significantly induce stress and strain inside the distorted lattice [72,73]. Additionally, the sample with x = 0.10 provided the highest microstrain value, indicating that this sample had the highest observed distortion which might be attributed to the high diffused calcium inside the PZT lattice, which is consistent with the obtained results of Rietveld refinement.

Tolerance factor. The term of the perovskite tolerance factor, t_o, was originally introduced by Goldschmidt and redesigned afterwards via many researchers, for example, Megaw [74] and Ubic [75], to represent the symmetry and structural stability of the perovskite materials for a specific sequence of ions and accordingly an insight into the mismatch between the bonding prerequisites of the A-site and B-site cations plus a quantitative evaluation of the structural distortion [76,77].

The Goldschmidt tolerance factor t_0 can be expressed as:

$$t_0 = \frac{r_{A(id)} + r_{O(id)}}{\sqrt{2}(r_{B(id)} + r_{O(id)})} \tag{2}$$

where $r_{A(id)}$, $r_{B(id)}$ and $r_{O(id)}$ are the effective Shannon [64] ionic radius of A, B and the oxygen ion, respectively. The t_0 was calculated for the synthesized compositions and is listed in Table 4. The ionic radius of the A-/B-site was determined according to the chemical formula of the compositions, taken into account that the Ti^{4+} and Zr^{4+} co-occupy the B-site whereas the Pb^{2+} and the Ca^{2+} co-occupy the A-site in the distorted lattice [31]. The obtained results of the prepared PCZT nanopowders show that the t_0 ranged from $t_0 = 0.994$ to $t_0 = 0.984$, implying a stable ferroelectric with distorted perovskite structure [1,31,76].

Recently, empirical modelling approaches for perovskite materials were developed [69,75] which account for the effect of A-site vacancies and oxygen vacancies. These models rely on the concepts that the increased amount of oxygen vacancies does not affect the B-site size, r_B, the oxygen anions are in contact with both the A-site and B-site cations, the effective r_O is a function of t_0 and that the effective r_A is a function of both the concentration of A-site vacancies and t_0. According to these revised models, the modified perovskite tolerance factor t^* can be defined as [75]:

$$t^* = \frac{a_{pc} - 0.011730139}{0.7209203(r_{B(id)} + r_O)} - 1.760998 \tag{3}$$

where a_{pc}, $r_{B(id)}$, and r_O are the pseudocubic lattice constant, the effective Shannon ionic radius of B ion, and the effective ionic radius of oxygen ion, respectively. There is though a distinct advantage of the modified tolerance factor, t^*, over Goldschmidt tolerance factor, t_0, in

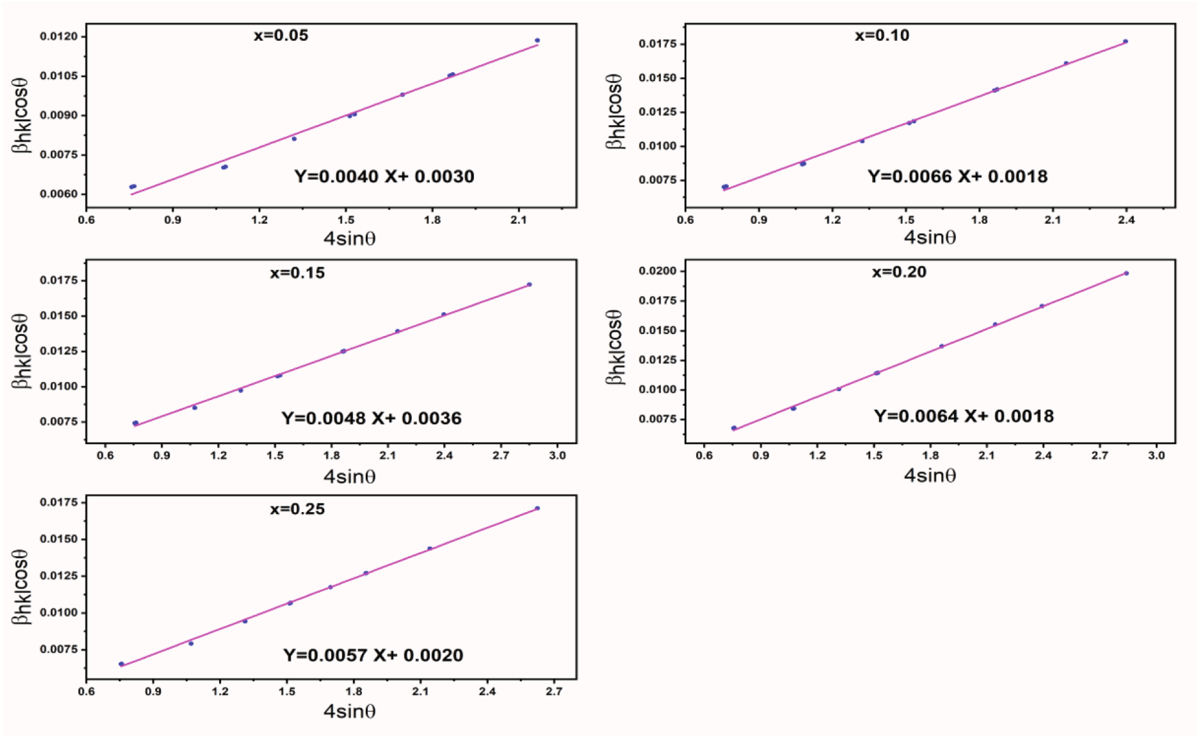

Fig. 5. Williamson–Hall (WH) plots for $Pb_{(1-x)}Ca_xZr_{0.52}Ti_{0.48}O_3$ nanopowders.

Table 3
Crystallite size and lattice microstrain values estimated by WH, and Rietveld methods of PCZT nanopowders.

x (Mole Fraction)	Rietveld		WH	
	Size (nm)	Strain	Size (nm)	Strain
0.05	42.62	0.0069	47.69	0.0040
0.10	41.76	0.0089	79.66	0.0066
0.15	56.04	0.0074	38.94	0.0048
0.20	42.44	0.0077	78.76	0.0064
0.25	45.34	0.0078	69.06	0.0057

that it provides the tolerance factor without prior knowledge of r_A and predicts octahedral distortions more effectively than does t_0. As a result, it takes out the imprecision in estimating effective sizes of partially-occupied A sites which are of importance in the current study [69].

The pseudocubic lattice constant can be determined from the relation [69]:

$$a_{pc} = \left(\frac{V}{Z}\right)^{1/3} \quad (4)$$

where V is the unit-cell volume and Z is the number of ABO_3 formula units within the unit cell. The effective size of the oxygen anion, r_O, can be defined as [69]:

$$r_O = \frac{a_{pc}}{2} - r_{B(id)} \quad (5)$$

where $r_{B(id)}$ is the Shannon ionic radius of the B-site cation in six-fold coordination. The effective size of oxygen vacancies r_{V_O} is related to the modified tolerance factor t^* by the following expression [69]:

$$r_{V_O} = -305.775864(t^*)^3 + 863.428549(t^*)^2 - 813.609546(t^*) + 257.011523 \quad (6)$$

In addition, the effective size of lead (Pb) vacancies r_{VPb} is related to the Goldschmidt tolerance factor, t_0, by the following expression [75]:

$$r_{VPb} = -20.8796 + 36.9049t_0 - 14.4590t_0^2 \quad (7)$$

Table 4 summarizes the results of Goldschmidt tolerance factor (t_o), modified tolerance factor (t*), and effective vacancy size (rV) for A-site and O-site. The obtained results indicate that the Goldschmidt tolerance factor decreases as the calcium concentration (x) increases which is expected as the ionic radius of the A-site decreases with the increase of the x concentration. On the other hand, the modified tolerance factor shows an interesting tendency, where first slightly decreased up to x = 0.10 and dramatically increased afterwards with the increase of x concentration. The reason behind this is that the modified tolerance factor calculations depend on the pseudocubic lattice constant (a_{pc}), which in turn depends on the unit cell volume. On the one hand, the effective size

Table 4
Summary of the obtained results of the tolerance factors for the synthesized PCZT nanopowders.

x (Mole Fraction)	rA(id) (Å)	t_o	V ($Å^3$)	a_{pc} (Å)	rO (Å)	t*	rV for O-site	rV for Pb-site
0 (♣)	1.4900	0.9967	67.5350	4.0723	1.3714	1.00524	1.0317	1.540
0.05	1.4825	0.9941	66.2400	4.0461	1.3583	1.00519	1.0320	1.519
0.10	1.4750	0.9915	65.9900	4.0410	1.3557	1.00518	1.0320	1.497
0.15	1.4675	0.9888	66.5800	4.0530	1.3617	1.00520	1.0319	1.475
0.20	1.4600	0.9862	67.2800	4.0672	1.3688	1.00523	1.0318	1.453
0.25	1.4525	0.9836	67.4300	4.0702	1.3703	1.00524	1.0318	1.431

(♣) Refers To The PDF Card No.: 00-033-0784.

of oxygen vacancies slightly increased up to x = 0.10 and then dramatically decreased with the increase of x concentration, while the effective size of lead vacancies decreased the increase of x concentration. It is noteworthy again that the calculated values of the modified tolerance factor for all of the synthesized PCZT nanopowders are extremely close to unity (t*= 1.005), which indicate strong stability of the ferroelectric perovskite structure [1,76]. These results suggest that the calcium ion is a good candidate to partially substitute the lead ion in the PZT system. Further studies with ferroelectric and piezoelectric experiments are needed to confirm that hypothesis.

SEM, TEM and elemental analysis

The scanning electron microscopy (SEM) images of the synthesized PCZT at x = 0.15 are displayed in Fig. 6 (a and b) which demonstrates that the morphology of most particles seems to be spherical in nature with a diameter in the nanometre scale along with the appearance of a rod-like granular structure, refer to the arrow. The transmission electron microscopy (TEM) technique was also used to investigate the internal particles microstructure for the sample with x = 0.15, as shown in Fig. 6 (c) which shows that the shapes of the particles have slightly changed with the occurrence of the rod-like agglomerates in comparison with the earlier observed results [24]. Moreover, it is obvious from the micrograph that the granules pretend to be agglomerated when accumulated into the grid with irregular shape distribution. Cho [23] proposed that the presence of nontransformed precursors in free granules can give rise to agglomerated grains. X-ray fluorescence spectroscopy (XRF) study was carried out for nanopowders with x = 0.05 and presented in Fig. 6 (d). The XRF spectrum shows intensive peaks of Pb, in addition to the emission lines of Zr, Ti, and Ca. It is evident from the spectrum that the obtained nanopowder did not show any emission lines for other elements, which reflect the pureness of the formed PCZT nanopowders. The particle sizes perceived from TEM images are further consistent with those evaluated throughout the Rietveld refinement and WH methods for the specimen with x = 0.15.

FT-IR study

FT-IR studies of calcium doped lead zirconate titanate compositions have been performed. Supplementary Fig. S1 provides the results derived from the preliminary analysis of the compound with x = 0.05. The spectrum shows that the strong observed broad band in the range from 480 cm^{-1} to 700 cm^{-1} relates to M-O-M bonds (M = Zr, Ti, Ca, and Pb), whereby the formation of perovskite-type structure could be emphasized [78,79]. The bands situated at 1430 cm^{-1} and 1120 cm^{-1} correspond to C-O bond antisymmetrical stretching vibration and CO_3^{2-} stretching band, respectively [49,80], while the wide band ranging from 3400 cm^{-1} to 3800 cm^{-1} corresponds to the O–H stretching vibration band of modes of water molecules, which is consistent with earlier reports [63,79].

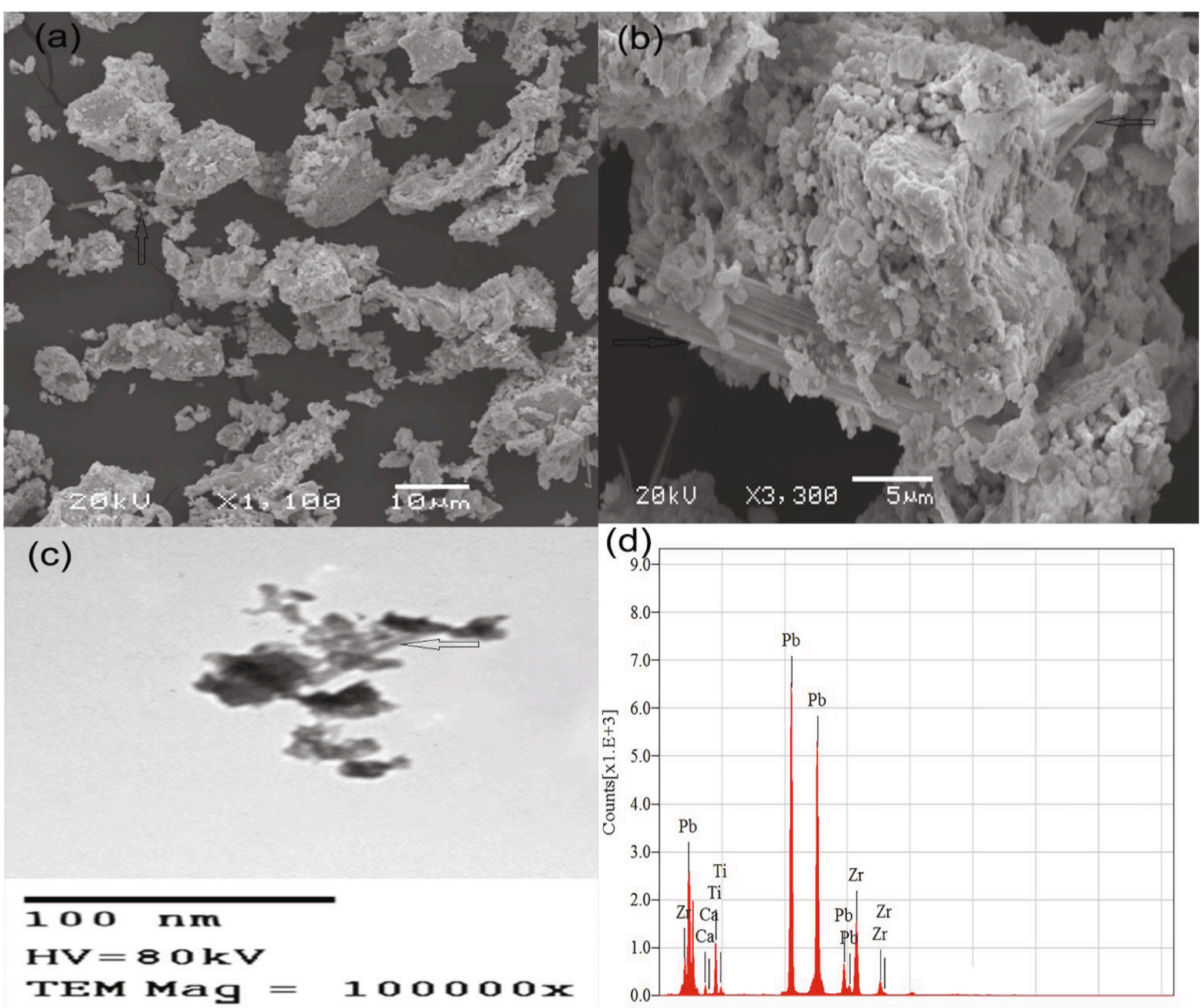

Fig. 6. (a-b), and (c) are the SEM, and the TEM images of $Pb_{0.85}Ca_{0.15}Zr_{0.52}Ti_{0.48}O_3$, while (d) is the XRF of $Pb_{0.95}Ca_{0.05}Zr_{0.52}Ti_{0.48}O_3$ synthesised nanopowders, respectively.

Optical properties

The optical properties of the synthesized nanopowders were investigated through measuring the optical diffused reflectance spectra (DRS). The DRS measurements were performed in the range from 200 nm to 1100 nm, and they are displayed in Supplementary Fig. S2. The evaluation of the optical band gap was performed through the use of diffuse reflectance measurements for the powder materials which are considered more suitable technique compared to the absorbance measurements since the absorption assessments do not reveal the exact judgement of the optical gap and might end up in mistaken conclusions, whereas the reflection assessments have a value beyond the absorption measurements due to the certainty of the strengthening of the scattering phenomenon that is arising in the powder materials [81].

The DRS spectra signify a wide and obvious absorption band with the highest absorption at ~340–370 nm. This wide absorption band centered at ~350 nm is assigned to the movement from the valence band to the conduction band. For evaluating the optical gap energy, the transformed Kubelka-Munk function F(R) was employed, as illustrated earlier in [53,82]. In fact, the Kubelka-Munk paradigm is fine when the particle size is lower or close to the wavelength of the used beam, and the proportions of the refraction, reflection, and diffraction are no longer approved to be separated through the diffused reflection which implies that the scattering should occur [81]. Consequently, the Kubelka-Munk function is generally functional for considerably light scattering material.

The optical energy gap (E_g) is correlated with the linear absorption coefficient (α) of a specific substance using the published Tauc relation, as given in the following equation:

$$\alpha h\nu = A_1\left(h\nu - E_g\right)^r \tag{8}$$

where $h\nu$ is the photon energy, A_1 is a proportion constant, and r depends on the optical transition type. The value of r is $\frac{1}{2}$ for direct allowed transitions, 2 for indirect allowed transitions, $\frac{3}{2}$ for direct forbidden transitions, and 3 for indirect forbidden transitions [83]. A modified Kubelka-Munk function can be obtained taking into consideration that the scattering coefficient is constant as regards the wavelength of the incident beam.

$$\left(F(R)h\nu\right)^{1/r} = A_2\left(h\nu - E_g\right) \tag{9}$$

In the present case, the plots of $(F(R)h\nu)^2$, $(F(R)h\nu)^{1/2}$, $(F(R)h\nu)^{2/3}$, and $(F(R)h\nu)^{1/3}$ as a function of the photon energy $h\nu$ were constructed [81]. It is found that the best fitting was achieved for $r = 1/2$ in Eq. (9), that is, $(F(R)h\nu)^2$ with respect to the photon energy ($h\nu$) implying that the occurred band transition is essentially direct allowed transition, as proposed by Tauc et al., and this agrees well with the previously reported studies [53,63].

The values of the optical gap for the prepared nanopowder samples were evaluated from the intersection of the linear fit for the linear section with the photon energy $h\nu$ axis, where $(F(R)h\nu)^2 = 0$, as shown in Fig. 7. The calculated optical band gap was 3.18, 3.12, 3.04, 3.03, and 3.08 eV for the synthesized PCZT nanopowders with the compositions of x = 0.05, 0.1, 0.15, 0.20, and 0.25, respectively. It is noticeable that the evaluated band gap (Eg) values significantly decreased from 3.22 eV for x = 0 to 3.03 eV for x = 0.20 and thereafter slightly increased to 3.08 eV with the further increase in ×, as presented in Fig. 8(a). The observed narrowing of optical energy gap could be attributed to the insertion of Ca^{2+} in the lead site of lead zirconate titanate that is might also be accountable for the formation of states within the conduction band as a result of the difference in hybridization between Ca_{4s}-O_{2p} and Pb_{6s}-O_{2p} [84,85]. In addition, the partial substitution of Pb^{2+} by Ca^{2+} and the subsequent evolution of PbO, and $CaTiO_3$ phases is expected to produce higher disorder leading to the creation of vacancy defects that is directly effect the electronic structure of the synthesised material and hence the reduction of the bandgap through the creation of defect levels within the band gap, i.e. lower than the conduction band edge and higher than the valence band edge [82,86]. It is also interesting to note that the calcium titanate with extremely small crystallite sizes will have a wider band gap around 3.5 to 3.85 eV [87,88], which might be responsible for the later increase of the optical band with further increase in x (calcium concentration). These observations greatly corroborate with the findings of the Rietveld structure refinements.

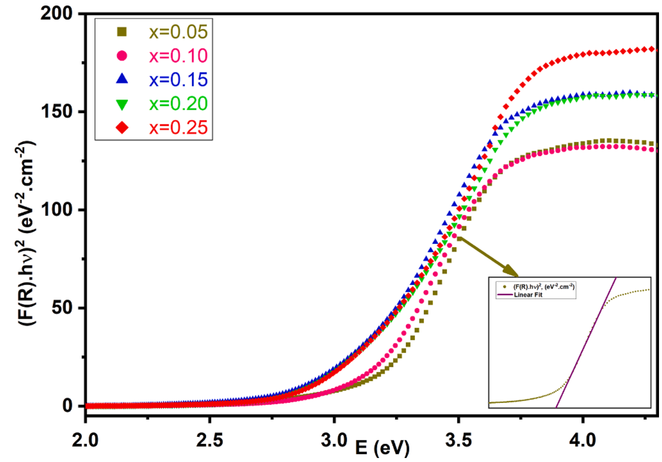

Fig. 7. Kubelka–Munk plots for band gap evaluation of the synthesised PCZT nanopowders heat treated at 750 °C for 3 h in air.

The variation of the band gap as regards the fractional percent of PZT-Tet, and $CaTiO_3$-Orth is illustrated in Fig. 8(b) which demonstrates that the band gap is greatly influenced by the presence of the $CaTiO_3$ and the PZT phases with a general trend, where the band gap first decreased gradually and later increased at a specific point. In Addition, a more detailed observation exhibits that the energy gap is significantly affected by the partial substitution of Pb^{2+} by Ca^{2+} and the subsequent evolution of the $CaTiO_3$ phase in comparison with the presence of the PbO phase. This result might be due to the marked difference on the optical band of these two phases, where the optical gap value of the tetragonal PbO is 1.9 eV [89], and it is about 3.6 eV for the orthorhombic $CaTiO_3$ [90].

Conclusion

Perovskite-type $Pb_{(1-x)}Ca_xZr_{0.52}Ti_{0.48}O_3$(PCZT) material with x = 0.05, 0.10, 0.15, 0.20, and 0.25 was successfully synthesized through the use of the polymeric precursor route. The XRD, TGA/DSC, UV–VIS, FT-IR, SEM, TEM, and XRF techniques were utilized for investigating the effects of substituting lead ions (Pb^{2+}) by calcium ions (Ca^{2+}) in PZT system on the structural and optical aspects. The TGA/DSC measurement revealed that the formation of the perovskite structure begins at 600 °C. The formation of the tetragonal PZT for all the prepared compositions was confirmed by the XRD analysis, while the orthorhombic $CaTiO_3$ was found to first appear at the composition of x = 0.15 and was growing as x increased. It was found that the PZT unit cell parameters and volume obtained from Rietveld refinements decreased up to x = 0.10 concentration and then gradually increased as calcium concentration increased. Furthermore, the crystallite size values obtained from Rietveld refinements showed the opposite trend of the WH values. The modified tolerance factor values were extremely close to unity, indicating a strong ferroelectric perovskite structure. Nevertheless, the formation of particles in the nanometers scale was confirmed by the TEM micrographs, whereas the XRF proved the absence of the impurities in the prepared samples. Furthermore, the SEM images demonstrated the appearance of rod-like particles in the nanopowder sample of the x = 0.15 concentration. The FT-IR spectrum exhibited the formation of the perovskite structure. The optical band gap energy reduced from 3.18 eV

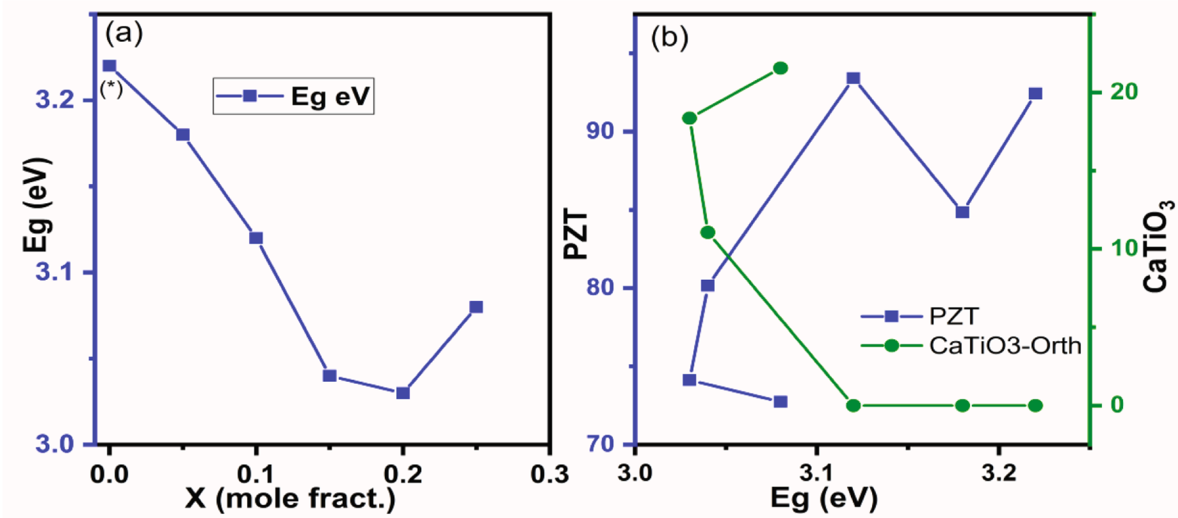

(*) this value from our previous work [24].

Fig. 8. variation of band gap with respect to (a) Ca concentration and (b) fractional percent of PZT, and $CaTiO_3$.

for x = 0.05 to 3.03 eV for x = 0.20 and increased to some extent afterwards to 3.08 eV for the composition of x = 0.25.

CRediT authorship contribution statement

K.H. Omran: . : Conceptualization, Methodology, Formal analysis, Data curation, Visualization, Writing - original draft, Writing - review & editing. **M. Mostafa:** Methodology, Validation, Writing - review & editing. **M.S. Abd El-sadek:** Methodology, Validation, Writing - review & editing. **O.M. Hemeda:** Conceptualization, Visualization, Validation, Supervision, Writing - review & editing. **R. Ubic:** Visualization, Validation, Writing - review & editing.

Declaration of Competing Interest

The authors declare that they have no known competing financial interests or personal relationships that could have appeared to influence the work reported in this paper.

Appendix A. Supplementary data

Supplementary data to this article can be found online at https://doi.org/10.1016/j.rinp.2020.103580.

References

[1] Panda PK, Sahoo B. PZT to lead free piezo ceramics: a review. Ferroelectrics 2015;474:128–43. https://doi.org/10.1080/00150193.2015.997146.
[2] Manjón-Sanz AM, Dolgos MR. Applications of piezoelectrics: old and new. Chem Mater 2018;30:8718–26. https://doi.org/10.1021/acs.chemmater.8b03296.
[3] Surendran KP, Ubic R. Perovskites. Microw. Mater. Appl. 2V Set, Chichester, UK: John Wiley & Sons, Ltd; 2017, p. 81–148. doi: 10.1002/9781119208549.ch3.
[4] Lozano-Sánchez LM, Lee S-W, Sekino T, Rodríguez-González V. Practical microwave-induced hydrothermal synthesis of rectangular prism-like CaTiO3. CrystEngComm 2013;15:2359. https://doi.org/10.1039/c3ce27040h.
[5] Ghoneim MT, Zidan MA, Alnassar MY, Hanna AN, Kosel J, Salama KN, et al. Thin PZT-based ferroelectric capacitors on flexible silicon for nonvolatile memory applications. Adv Electron Mater 2015;1:1–10. https://doi.org/10.1002/aelm.201500045.
[6] Dong L, Jin C, Closson AB, Trase I, Richards HC, Chen Z, et al. Cardiac energy harvesting and sensing based on piezoelectric and triboelectric designs. Nano Energy 2020;76:105076. https://doi.org/10.1016/j.nanoen.2020.105076.
[7] Ibn-Mohammed T, Koh SCL, Reaney IM, Acquaye A, Wang D, Taylor S, et al. Integrated hybrid life cycle assessment and supply chain environmental profile evaluations of lead-based (lead zirconate titanate) versus lead-free (potassium sodium niobate) piezoelectric ceramics. Energy Environ Sci 2016;9:3495–520. https://doi.org/10.1039/C6EE02429G.
[8] Ibn-Mohammed T, Koh SCL, Reaney IM, Sinclair DC, Mustapha KB, Acquaye A, et al. Are lead-free piezoelectrics more environmentally friendly? MRS Commun 2017;7:1–7. https://doi.org/10.1557/mrc.2017.10.
[9] Ibn-Mohammed T, Reaney IM, Koh SCL, Acquaye A, Sinclair DC, Randall CA, et al. Life cycle assessment and environmental profile evaluation of lead-free piezoelectrics in comparison with lead zirconate titanate. J Eur Ceram Soc 2018;38:4922–38. https://doi.org/10.1016/j.jeurceramsoc.2018.06.044.
[10] Banerjee A, Bandyopadhyay A, Bose S. Influence of La2O3, SrO, and ZnO Addition on PZT. J Am Ceram Soc 2006;89:1594–600. https://doi.org/10.1111/j.1551-2916.2006.00927.x.
[11] Schmitt LA, Kungl H, Hinterstein M, Riekehr L, Kleebe HJ, Hoffmann MJ, et al. The impact of heat treatment on the domain configuration and strain behavior in Pb[Zr, Ti]O-3 ferroelectrics. J Am Ceram Soc 2015;98:269–77. https://doi.org/10.1111/jace.13253.
[12] Araújo EB, Lima EC, Guerra JDS, dos Santos AO, Cardoso LP, Kleinke MU. Evidence for the monoclinic–tetragonal phase coexistence in Pb(Zr 0.53 Ti 0.47)O 3 thin films. J Phys Condens Matter 2008. https://doi.org/10.1088/0953-8984/20/41/415203.
[13] Zhang N, Yokota H, Glazer AM, Ren Z, Keen DA, Keeble DS, et al. The missing boundary in the phase diagram of PbZr1-xTixO3. Nat Commun 2014;5:1–9. https://doi.org/10.1038/ncomms6231.
[14] Ragini MSK, Pandey D, Lemmens H, Van TG. Evidence for another low-temperature phase transition in tetragonal Pb(ZrxTi1-x)O3 (x=0.515,0.520). Phys Rev B 2001. https://doi.org/10.1103/PhysRevB.64.054101.
[15] Nguyen MD, Trinh TQ, Dekkers M, Houwman EP, Vu HN, Rijnders G. Effect of dopants on ferroelectric and piezoelectric properties of lead zirconate titanate thin films on Si substrates. Ceram Int 2014;40:1013–8. https://doi.org/10.1016/j.ceramint.2013.06.098.
[16] Holman RL, Fulrath RM. Intrinsic nonstoichiometry in the lead zirconate-lead titanate system determined by Knudsen effusion. J Appl Phys 1973;44:5227–36. https://doi.org/10.1063/1.1662136.
[17] Majumder SB, Mohapatra YN, Agrawal DC. Optical and microstructural characterization of sol-gel derived cerium-doped PZT thin films. J Mater Sci 1997;32:2141–50.
[18] Gueye I, Le Rhun G, Gergaud P, Renault O, Defay E, Barrett N. Chemistry of surface nanostructures in lead precursor-rich PbZr0.52Ti0.48O3sol-gel films. Appl Surf Sci 2016;363:21–8. https://doi.org/10.1016/j.apsusc.2015.11.118.
[19] Jha P, Arya P, Ganguli A. Dielectric properties of lead zirconium titanates with nanometer size grains synthesized by the citrate precursor route. Mater Chem Phys 2003;82:355–61. https://doi.org/10.1016/S0254-0584(03)00266-9.
[20] Siddiqui M, Mohamed JJ, Ahmad ZA. Structural, piezoelectric, and dielectric properties of PZT-based ceramics without excess lead oxide. J Aust Ceram Soc 2020;56:371–7. https://doi.org/10.1007/s41779-019-00337-3.
[21] Pechini MP. Method of preparing lead and alkaline earth titanates and niobates and coating method using the same to form a capacitor. US3330697, 1967.
[22] Prado LR, de Resende NS, Silva RS, Egues SMS, Salazar-Banda GR. Influence of the synthesis method on the preparation of barium titanate nanoparticles. Chem Eng Process Process Intensif 2016;103:12–20. https://doi.org/10.1016/j.cep.2015.09.011.
[23] Cho W-S. Structural evolution and characterization of BaTiO3 nanoparticles synthesized from polymeric precursor. J Phys Chem Solids 1998;59:659–66. https://doi.org/10.1016/S0022-3697(97)00227-8.
[24] Omran KH, El-sadek MSA, Mostafa M, Hemeda OM. Influence of PbO phase content on structural and optical properties of PZT nanopowders. Appl Nanosci 2020;10:2315–27. https://doi.org/10.1007/s13204-020-01390-2.

[25] Teixeira GF, Lustosa GMMM, Zanetti SM, Zaghete MA. Chemical synthesis and epitaxial growth methods for the preparation of ferroelectric ceramics and thin films. Magn Ferroelectr Multiferroic Met Oxides 2018:121–37. https://doi.org/10.1016/B978-0-12-811180-2.00006-2.

[26] Yashima M, Hoshina T, Ishimura D, Kobayashi S, Nakamura W, Tsurumi T, et al. Size effect on the crystal structure of barium titanate nanoparticles. J Appl Phys 2005;98:014313. https://doi.org/10.1063/1.1935132.

[27] Chaput F, Boilot J-P, Beauger A. Alkoxide-hydroxide route to syntheltize BaTiO3-based powders. J Am Ceram Soc 1990;73:942–8. https://doi.org/10.1111/j.1151-2916.1990.tb05141.x.

[28] Liu W, Liu W, Wang Y, Xue C, Wang J, Yang J. Piezoelectric and mechanical properties of CaO reinforced porous PZT ceramics with one-dimensional pore channels. Ceram Int 2017;43:2063–8. https://doi.org/10.1016/j.ceramint.2016.10.181.

[29] Bochenek D, Niemiec P, Dercz G. The effect of mixed doping on the microstructure and electrophysical parameters of the multicomponent PZT-type ceramics. Materials (Basel) 2020;13:1996. https://doi.org/10.3390/ma13081996.

[30] Bhattarai MK, Pavunny SP, Instan AA, Scott JF, Katiyar RS. Effect of off-center ion substitution in morphotropic lead zirconate titanate composition. J Appl Phys 2017;121:194102. https://doi.org/10.1063/1.4983526.

[31] Chen Y, Zhou H, Wang S, Chen Q, Wang Q, Zhu J. Diffused phase transition, ionic conduction mechanisms and electric-field dependent ferroelectricity of Nb/Ce co-doped Pb(Zr0.52Ti0.48)O3 ceramics. J Alloys Compd 2020. https://doi.org/10.1016/j.jallcom.2020.155500.

[32] Shannigrahi SR, Tay FEH, Yao K, Choudhary RNP. Effect of rare earth (La, Nd, Sm, Eu, Gd, Dy, Er and Yb) ion substitutions on the microstructural and electrical properties of sol-gel grown PZT ceramics. J Eur Ceram Soc 2004;24:163–70. https://doi.org/10.1016/S0955-2219(03)00316-9.

[33] Amarande L, Miclea C, Cioangher M, Grecu MN, Pasuk I. Effects of vanadium doping on sintering conditions and functional properties of Nb Li co-doped PZT ceramics. Comments on Li location. J Alloys Compd 2016;685:159–66. https://doi.org/10.1016/j.jallcom.2016.05.266.

[34] Bochenek D, Niemiec P, Ćwikiel E, Goryczka T. PZT-type ceramics doped with manganese, antimony, lanthanum and tungsten – technology and physical properties. Arch Metall Mater 2020;65:827–37. https://doi.org/10.24425/amm.2020.132828.

[35] Sahoo B, Panda PK. Ferroelectric, dielectric and piezoelectric properties of Pb1−x Ce x (Zr0.60Ti0.40)O3, $0 \le x \le 0.08$. J Mater Sci 2007;42:9684–8. https://doi.org/10.1007/s10853-007-1948-4.

[36] Nasar R, Cerqueira M, Longo E, Varela J, Beltran A. Experimental and theoretical study of the ferroelectric and piezoelectric behavior of strontium-doped PZT. J Eur Ceram Soc 2002;22:209–18. https://doi.org/10.1016/S0955-2219(01)00256-4.

[37] Haertling GH. Ferroelectric ceramics: History and technology. J Am Ceram Soc 1999;82:797–818. https://doi.org/10.1111/j.1151-2916.1999.tb01840.x.

[38] Kulcsar F. Electromechanical properties of lead titanate zirconate ceramics with lead partially replaced by calcium or strontium. J Am Ceram Soc 1959;42:49–51. https://doi.org/10.1111/j.1151-2916.1959.tb09141.x.

[39] Cerqueira M, Nasar RS, Longo E, Varela JA, Beltrán A, Llusar R, et al. Piezoelectric behaviour of PZT doped with calcium: a combined experimental and theoretical study. J Mater Sci 1997;32:2381–6. https://doi.org/10.1023/A:1018501022807.

[40] Tawfik A, Eatah AI, Abd E-S. Dielectric and electromechanical properties of calcium-doped lead zirconate titanate. Mater Sci Eng 1983;60:145–9. https://doi.org/10.1016/0025-5416(83)90184-2.

[41] Sachdeva A, Luthra V, Gautam P, Tandon RP. Dielectric and ferroelectric studies on sol-gel derived calcium modified lead zirconate titanate ceramics. Integr Ferroelectr 2010;122:74–82. https://doi.org/10.1080/10584587.2010.492289.

[42] Kour P, Kumar P, Sinha SKK, Kar M. Electrical properties of calcium modified PZT (52/48) ceramics. Solid State Commun 2014;190:33–9. https://doi.org/10.1016/j.ssc.2014.03.025.

[43] Kour P, Pradhan SK, Kumar P, Sinha SK, Kar M. Study of ferroelectric and piezoelectric properties on Ca doped PZT ceramics. Mater Today Proc 2017;4:5727–33. https://doi.org/10.1016/j.matpr.2017.06.037.

[44] Nasar RS, Cerqueira M, Longo E, Varela JA. Analysis of Ca-PZT powder obtained by the Pechini and partial oxalate methods. Cerâmica 2008;54:38–42. https://doi.org/10.1590/S0366-69132008000100006.

[45] Zhuang ZQ, Haun MJ, Jang S-J, Cross LE. Composition and temperature dependence of the dielectric, piezoelectric and elastic properties of pure PZT ceramics. IEEE Trans Ultrason Ferroelectr Freq Control 1989;36:413–6. https://doi.org/10.1109/58.31777.

[46] Ounaies Z. Sol-gel and microwave processing of pzt materials for sensor and actuator applications. 1995.

[47] Mahmood A, Naeem A, Iqbal Y, Ullah A. Dielectric and ferroelectric properties of the sol-gel-derived Zr-doped $Ba_{0.7}$ $Sr_{0.3}$ TiO_3 polycrystalline ceramic systems. Int J Appl Ceram Technol 2017;14:604–10. https://doi.org/10.1111/ijac.12678.

[48] Rai AK, Mandal KD, Kumar D, Parkash O. Dielectric properties of lanthanum-doped CaCu3Ti4O12 synthesized by semi-wet route. J Phys Chem Solids 2009;70:834–9. https://doi.org/10.1016/J.JPCS.2009.04.001.

[49] Arya PR, Jha P, Ganguli AK. Synthesis, characterization and dielectric properties of nanometer-sized barium strontium titanates prepared by the polymeric citrate precursor method. J Mater Chem 2003;13:415–23. https://doi.org/10.1039/b205087k.

[50] Ianculescu AC, Vasilescu CA, Crisan M, Raileanu M, Vasile BS, Calugaru M, et al. Formation mechanism and characteristics of lanthanum-doped BaTiO3 powders and ceramics prepared by the sol-gel process. Mater Charact 2015;106:195–207. https://doi.org/10.1016/j.matchar.2015.05.022.

[51] Khorrami GHH, Khorsand Zak A, Banihashemian SMM, Zak AK, Banihashemian SMM. Magnetic and dielectric properties on sol-gel combustion synthesis of Pb(Zr0.52, Ti0.43X0.05)O3(X = Fe, Ni, and Co) nanoparticles. Adv Powder Technol 2014;25:1319–24. https://doi.org/10.1016/j.apt.2014.03.011.

[52] Lakeman CDE, Payne DA. Processing effects in the sol-gel preparation of PZT dried gels, powders, and ferroelectric thin layers. J Am Ceram Soc 1992;75:3091–6. https://doi.org/10.1111/j.1151-2916.1992.tb04392.x.

[53] Samanta S, Sankaranarayanan V, Sethupathi K. Band gap, piezoelectricity and temperature dependence of differential permittivity and energy storage density of PZT with different Zr/Ti ratios. Vacuum 2018;156:456–62. https://doi.org/10.1016/j.vacuum.2018.08.015.

[54] Kumar P, Singh P, Singh S, Juneja JK, Prakash C, Raina KK. Influence of lanthanum substitution on dielectric properties of modified lead zirconate titanates. Ceram Int 2015;41:5177–81. https://doi.org/10.1016/j.ceramint.2014.12.017.

[55] Samanta S, Muralidhar M, Sankaranarayanan V, Sethupathi K, Ramachandra Rao MS, Murakami M. Band gap reduction and redshift of lattice vibrational spectra in Nb and Fe co-doped PLZT. J Mater Sci 2017;52:13012–22. https://doi.org/10.1007/s10853-017-1425-7.

[56] M. J, Rivera-Ruedas G, De Jesus FS, M. A, Jimenez R, Munoz-Saldan J. Synthesis of PZT Ceramics by Sol-Gel Method and Mixed Oxides with Mechanical Activation Using Different Oxides as a Source of Pb. Ferroelectr. – Mater. Asp., InTech; 2011, p. 331–46. doi: 10.5772/18125.

[57] Zak AK, Majid WHA. Effect of solvent on structure and optical properties of PZT nanoparticles prepared by sol–gel method, in infrared region. Ceram Int 2011;37:753–8. https://doi.org/10.1016/j.ceramint.2010.10.020.

[58] Rodríguez-Aranda MC, Calderón-Piñar F, Hernández-Landaverde MA, Heiras J, Zamorano-Ulloa R, Ramírez-Rosales D, et al. Photoluminescence of sol–gel synthesized PZT powders. J Lumin 2016;179:280–6. https://doi.org/10.1016/J.JLUMIN.2016.07.030.

[59] Mandal TK. Rietveld refinement on XRD and TEM study of nanocrystalline PbZr0:5Ti0:5O3 ceramics prepared with a soft chemistry route. Mater Sci 2015;33:18–24. https://doi.org/10.1515/msp-2015-0040.

[60] Chen X, Xu Y, Zhao C, Wang L, Wen S, Shi Y, et al. A highly enhanced photoluminescence of Eu3+-activated CaTiO3 phosphors via selective A-site and B-site cation substitutions (Sr2+ and Sn4+). J Electron Mater 2020;49:1969–79. https://doi.org/10.1007/s11664-019-07896-y.

[61] Kumar L, Kumar P, Kar M. Influence of Mn substitution on crystal structure and magnetocrystalline anisotropy of nanocrystalline Co1−xMn x Fe2−2xMn2xO4. Appl Nanosci 2013;3:75–82. https://doi.org/10.1007/s13204-012-0071-2.

[62] Nath D, Singh F, Das R. X-ray diffraction analysis by Williamson-Hall, Halder-Wagner and size-strain plot methods of CdSe nanoparticles- a comparative study. Mater Chem Phys 2020;239:122021. https://doi.org/10.1016/j.matchemphys.2019.122021.

[63] Ghasemifard M, Hosseini SM, Khorsand Zak A, Khorrami GH. Microstructural and optical characterization of PZT nanopowder prepared at low temperature. Phys E Low-Dimensional Syst Nanostructures 2009;41:418–22. https://doi.org/10.1016/J.PHYSE.2008.09.017.

[64] Shannon RD. Revised effective ionic radii and systematic studies of interatomic distances in halides and chalcogenides. Acta Crystallogr Sect A 1976;32:751–67. https://doi.org/10.1107/S0567739476001551.

[65] Jaimeewong P, Sittinon S, Buntham S, Bomlai P, Namsar O, Pojprapai S, et al. Ferroelectric, piezoelectric and dielectric behaviors of CoO- and Fe2O3-doped BCZT ceramics. Phys Status Solidi Appl Mater Sci 2018;215:1–6. https://doi.org/10.1002/pssa.201701023.

[66] Kamarulzaman N, Chayed NF, Badar N, Kasim MF, Mustaffa DT, Elong K, et al. Band gap narrowing of 2-D ultra-thin MgO graphene-like sheets. ECS J Solid State Sci Technol 2016;5:Q3038–45. https://doi.org/10.1149/2.0081611jss.

[67] Lozano-Sánchez LM, Obregón S, Díaz-Torres LA, Lee S-W, Rodríguez-González V. Visible and near-infrared light-driven photocatalytic activity of erbium-doped CaTiO3 system. J Mol Catal A Chem 2015;410:19–25. https://doi.org/10.1016/j.molcata.2015.09.005.

[68] Shivaram M, Nagabhushana H, Sharma SC, Prashantha SC, Daruka Prasad B, Dhananjaya N, et al. Synthesis and luminescence properties of Sm3+ doped CaTiO3 nanophosphor for application in white LED under NUV excitation. Spectrochim Acta Part A Mol Biomol Spectrosc 2014;128:891–901. https://doi.org/10.1016/j.saa.2014.02.117.

[69] Smith E, Škapin S, Ubic R. Correlative models for oxygen vacancies in perovskites. J Alloys Compd 2020;836:155475. https://doi.org/10.1016/j.jallcom.2020.155475.

[70] Muhammed Shafi P, Chandra Bose A. Impact of crystalline defects and size on X-ray line broadening: a phenomenological approach for tetragonal SnO 2 nanocrystals. AIP Adv 2015;5:057137. https://doi.org/10.1063/1.4921452.

[71] Omran KH, Abd El-sadek MS, Mostafa M, Hemeda OM. Microstructural analysis and optical properties of lead zirconate nanoparticles. JOM 2020. https://doi.org/10.1007/s11837-020-04296-0.

[72] Li Y, Zhang Z, Chen Y, Hall DA. Electric field-induced strain in core-shell structured BiFeO3–K0.5Bi0.5TiO3–PbTiO3ceramics. Acta Mater 2018;160:199–210. https://doi.org/10.1016/j.actamat.2018.08.033.

[73] Andreev YG, Bruce PG. Using crystallography to understand polymer electrolytes. J Phys Condens Matter 2001;13:8245–55. https://doi.org/10.1088/0953-8984/13/36/302.

[74] Megaw HD. Crystal structure of double oxides of the perovskite type. Proc Phys Soc 1946;58:133–52. https://doi.org/10.1088/0959-5309/58/2/301.

[75] Ubic R, Tolman K, Talley K, Joshi B, Schmidt J, Faulkner E, et al. Lattice-constant prediction and effect of vacancies in aliovalently doped perovskites. J Alloys Compd 2015;644:982–95. https://doi.org/10.1016/j.jallcom.2015.04.213.

[76] Ubic R, Tolman K, Chan K, Lundy N, Letourneau S, Kriven WM. Effective size of vacancies in aliovalently doped SrTiO3 perovskites. J Alloys Compd 2013;575:239–45. https://doi.org/10.1016/j.jallcom.2013.04.091.

[77] Yadav AK, Anita Kumar S, Reddy VR, Shirage PM, Biring S, et al. Structural and dielectric properties of Pb(1–x)(Na0.5Sm0.5)xTiO3 ceramics. J Mater Sci Mater Electron 2017;28:10730–8. https://doi.org/10.1007/s10854-017-6849-y.

[78] Yatish KV, Lalithamba HS, Suresh R, Latha HKE. Ochrocarpus longifolius assisted green synthesis of CaTiO3 nanoparticle for biodiesel production and its kinetic study. Renew Energy 2020;147:310–21. https://doi.org/10.1016/j.renene.2019.08.139.

[79] Bruncková H, Medvecký L, Briančin J, Saksl K. Influence of hydrolysis conditions of the acetate sol–gel process on the stoichiometry of PZT powders. Ceram Int 2004;30:453–60. https://doi.org/10.1016/S0272-8842(03)00131-7.

[80] Zhao Y, Zhang X, Li X, Lu Z, Zhu G, Liu L, et al. Monodispersed spherical Y2O3 and Y2O3:Eu3+ particles synthesized from modified homogeneous urea precipitation process. J Alloys Compd 2020;829:154562. https://doi.org/10.1016/j.jallcom.2020.154562.

[81] Kumar A, Dhoble SJ, Bhatt J, Terblans JJ, Swart HC. Structural characterization and influence of calcination temperature on luminescence properties of Sr0.91Mg2Al5.82Si9.18O30: Eu3+ nanophosphors. Powder Technol 2019;354:591–600. https://doi.org/10.1016/j.powtec.2019.06.031.

[82] Kumar R, Kumar A, Verma N, Khopkar V, Philip R, Sahoo B. Ni nanoparticles coated with nitrogen-doped carbon for optical limiting applications. ACS Appl Nano Mater 2020;3:8618–31. https://doi.org/10.1021/acsanm.0c01284.

[83] López R, Gómez R. Band-gap energy estimation from diffuse reflectance measurements on sol-gel and commercial TiO 2: a comparative study. J Sol-Gel Sci Technol 2012;61:1–7. https://doi.org/10.1007/s10971-011-2582-9.

[84] Rini EG, Paul A, Nasir M, Amin R, Gupta MK, Mittal R, et al. Correlation of octahedral distortion with vibrational and electronic properties of LaFe1-Ti O3 nanoparticles. J Alloys Compd 2020;830:154594. https://doi.org/10.1016/j.jallcom.2020.154594.

[85] Hussein RK, Bashter II, El-Okr M, Ibrahim MA. DFT investigation of structural and electronic properties of modified PZT. Acta Chem Iasi 2019;27:15–30. https://doi.org/10.2478/achi-2019-0002.

[86] Mahour LN, Choudhary HK, Kumar R, Anupama AV, Sahoo B. Structural, optical and Mössbauer spectroscopic investigations on the environment of Fe in Fe-doped ZnO (Zn1-xFexO) ceramics synthesized by solution combustion method. Ceram Int 2019;45:24625–34. https://doi.org/10.1016/j.ceramint.2019.08.194.

[87] Deng B, Si P, Bauman L, Luo J, Rao M, Peng Z, et al. Photocatalytic activity of CaTiO3 derived from roasting process of bauxite residue. J Clean Prod 2020;244:118598. https://doi.org/10.1016/j.jclepro.2019.118598.

[88] Moreira ML, Paris EC, do Nascimento GS, Longo VM, Sambrano JR, Mastelaro VR, et al. Structural and optical properties of CaTiO3 perovskite-based materials obtained by microwave-assisted hydrothermal synthesis: An experimental and theoretical insight. Acta Mater 2009;57:5174–85. doi: 10.1016/j.actamat.2009.07.019.

[89] Thangaraju B, Kaliannan P. Optical and structural studies on spray deposited α-PbO thin films. Semicond Sci Technol 2000;15:542–5. https://doi.org/10.1088/0268-1242/15/6/309.

[90] Zhuang J, Tian Q, Lin S, Yang W, Chen L, Liu P. Precursor morphology-controlled formation of perovskites CaTiO3 and their photo-activity for As(III) removal. Appl Catal B Environ 2014;156–157:108–15. https://doi.org/10.1016/j.apcatb.2014.02.015.